Electronic Supplementary Information: Machine Learning Real Space Microstructure Characteristics from Scattering Data

Matthew Jones, Nigel Clarke
Department of Physics & Astronomy, University of Sheffield, Hicks Building, Hounsfield Road, Sheffield S3 7RH, United Kingdom
(Dated: September 16, 2021)

I. SIMULATING POLYMERIC SPINODAL DECOMPOSITION

Polymeric spinodal decomposition was simulated in both two and three dimensions. The details of the simulations in both sets of dimensions differ because the simulation in two dimensions was aimed at the efficient generation of many time steps worth of data to test the ability of the Gaussian process regression models to make extrapolative predictions.

A. Three Dimensions

Spinodal decomposition was simulated in ten symmetric, binary, three-dimensional polymer blends with average compositions spanning the range $0.05 \leq \bar{\phi} \leq 0.5$ in increments of $\Delta\bar{\phi} = 0.05$. To do this, the following dimensionless form of the Cahn-Hilliard equation [1] [2] [3] was solved numerically using a finite difference scheme on a $256 \times 256 \times 256$ cubic lattice with periodic boundary conditions

$$\frac{\partial\phi(\mathbf{x},\tau)}{\partial\tau} = \nabla^2 \frac{\delta F(\phi(\mathbf{x},\tau))}{\delta\phi(\mathbf{x},\tau)} \tag{1a}$$

$$F = \frac{1}{(\chi_s - \chi)} \times \int \Big[\frac{1}{N}\ln\phi + \frac{1}{N}\ln(1-\phi) + \chi\phi(1-\phi)\Big] + \kappa\nabla^2\phi \; dV \tag{1b}$$

where ϕ is the volume fraction of one of the blend components, F is the Flory-Huggins-de Gennes (FHdG) free energy functional, $\delta/\delta\phi$ is a functional derivative, χ is the Flory-Huggins interaction parameter, with χ_s its value on the spinodal curve, N is the degree of polymerisation and $\kappa\boldsymbol{\nabla}^2\phi$ describes the energetic cost of gradients in composition. The value of χ_s is given by

$$\chi_s = \frac{1}{2N\bar{\phi}(1-\bar{\phi})}. \tag{2}$$

The FHdG free energy functional describes the free energy the system as the once homogeneous composition becomes non-uniform as a result of phase separation [1] [4] [5]. We note that the specific form of the FHdG free energy that we used, as shown above, does not impact qualitatively on the evolution of the microstructure.

$\bar{\phi}$	$\Delta\tau$
0.05	7.8125×10^{-6}
0.1	1.5625×10^{-5}
0.15	3.1250×10^{-5}
0.2-0.5	1.2500×10^{-4}

TABLE I: Average composition dependence of the time steps used in the finite difference scheme. Smaller time steps are required for smaller volume fractions to avoid numerical instabilities arising from the logarithmic terms in the free energy.

The dimensionless time and space variables, τ and $\mathbf{x}$, were related to real time and space, t and $\boldsymbol{x}$, through $\tau = D(\chi_s - \chi)^2 t/l^2$ and $\mathbf{x} = \sqrt{\chi - \chi_s}\boldsymbol{x}/l$ where D is a mutual diffusion coefficient and l is a characteristic molecular length scale, typically of the order of nanometers. The step size used in the finite difference scheme was $\Delta\mathrm{x} = 0.5$. The time steps are shown in table I. For each composition we set $N = 50$, $\kappa = 1/18$ and $(\chi - \chi_s) = 0.0254$. The cubic lattice was initialised such that the volume fraction at each site was $\phi = \bar{\phi} \pm \delta$ where δ is a uniformly distributed random variable in the range $-0.01 < \delta < 0.01$. In each simulation, the microstructure of the blend was saved at integer values of τ in the range $0 < \tau \leq 39$.

B. Two Dimensions

Spinodal decomposition was simulated in a single symmetric, binary, two-dimensional polymer blend with average composition $\bar{\phi} = 0.5$. To do this, the following dimensionless form of the Cahn-Hilliard equation was solved numerically using a finite difference scheme on a 256×256 square lattice with periodic boundary conditions

$$\frac{\partial\psi(\mathbf{x},\tau)}{\partial\tau} = \nabla^2\Big[-\psi + \frac{2}{3N(\chi-\chi_s)}\psi^3 - \nabla^2\psi\Big] \tag{3}$$

where $\psi \equiv 2\phi - 1$. This particular form of the Cahn-Hilliard was derived using the Ginzburg-Landau free energy functional and the de Gennes square gradient coefficient in the limit of a small interaction parameter [6] [5]. The dimensionless time and space variables, τ and $\mathbf{x}$, were related to real time and space, t and $\boldsymbol{x}$, through

$\tau = \frac{6\Lambda}{R_g^2}\frac{(\chi-\chi_s)^2}{\chi_s}t$ and $\mathbf{x} = \sqrt{\frac{3}{R_g^2}\Big[\frac{\chi}{\chi_s}-1\Big]}\boldsymbol{x}$ where Λ is an Onsager coefficient and R_g is the radius of gyration, typically of the order of nanometers. The spatial and temporal step sizes used in the finite difference scheme were $\Delta \mathrm{x} = 0.5$ and $\Delta\tau = 1 \times 10^{-3}$. We set $N = 10^3$ and $(\chi - \chi_s) = 0.001$. The square lattice was initialised such that $\psi = \bar{\psi} \pm \delta$ where δ is a uniformly distributed random variable in the range $-0.01 < \delta < 0.01$. The microstructure of the blend was saved at integer values of τ in the range $0 < \tau \leq 75$.

II. DETAILS ON THE COVARIANCE FUNCTIONS

The following summary of the covariance functions we used is based on information from Refs. [7] and [8].

Isotropic covariance functions are functions of $|\boldsymbol{x} - \boldsymbol{x'}|$ - they only depend on the magnitude of the difference between two inputs. The isotropic squared exponential covariance function is given by

$$\kappa_{SE}(\boldsymbol{x}, \boldsymbol{x'}) = \sigma^2 exp\Big(-\frac{|\boldsymbol{x} - \boldsymbol{x'}|^2}{2l^2}\Big) \tag{4}$$

where σ and l are both hyperparameters, which specify the shape of the covariance function. The hyperparameter σ is a scale factor and l is a characteristic length scale. The length scale is a particularly important hyperparameter because it determines how rapidly the functions f in the prior distribution of functions vary. The squared exponential covariance function gives rise to very smooth functions, with infinitely many derivatives. Such smooth functions are unrealistic in many applications, leading us now to consider the Matern class of covariance functions.

The isotropic Matern class of covariance functions are given by

$$\kappa_M(\boldsymbol{x}, \boldsymbol{x'}) = \sigma^2 \frac{2^{1-\nu}}{\Gamma(\nu)}\Big(\frac{\sqrt{2\nu}|\boldsymbol{x} - \boldsymbol{x'}|}{l}\Big)^{\nu} \kappa_\nu\Big(\frac{\sqrt{2\nu}|\boldsymbol{x} - \boldsymbol{x'}|}{l}\Big) \tag{5}$$

where ν is a positive parameter, $\Gamma(\nu)$ is the gamma function and K_ν is the modified Bessel function. The Matern class of covariance functions simplify for half-integer values of ν. Since when $\nu = 1/2$ the Matern covariance function gives rise to very rough functions, and when $\nu \geq 7/2$ it is hard to distinguish between the functions of the different Matern covariance functions, ν is often set to $\nu = 3/2$ or $\nu = 5/2$. In the case where $\nu = 1/2$, one obtains the exponential covariance function. The isotropic exponential covariance function is given by

$$\kappa_E(\boldsymbol{x}, \boldsymbol{x'}) = \sigma^2 exp\Big(-\frac{|\boldsymbol{x} - \boldsymbol{x'}|}{l}\Big). \tag{6}$$

Finally, we consider the rational quadratic covariance function. The rational quadratic covariance function is equivalent to adding together many squared exponential covariance functions with different length scales. The isotropic rational quadratic covariance function is given by

$$\kappa_{RQ}(\boldsymbol{x}, \boldsymbol{x'}) = \sigma^2 exp\Big(1 + \frac{|\boldsymbol{x} - \boldsymbol{x'}|^2}{2\alpha l^2}\Big)^{-\alpha} \tag{7}$$

where α is a hyperparameter that determines the relative weighting of the large and small length scale variations. It follows that the rational quadratic covariance function gives rise to smooth functions that vary across many length scales.

III. SUPPLEMENTARY RESULTS

A. Average Performance of All of the Models

Figures 1 - 3 show the average performance of the Gaussian process regression models at predicting the surface area, curvature and connectivity, respectively, from the original scattering data. In each figure, the top panel corresponds to the training set size of twenty training points, and the bottom panel corresponds to the training set size of thirty data points.

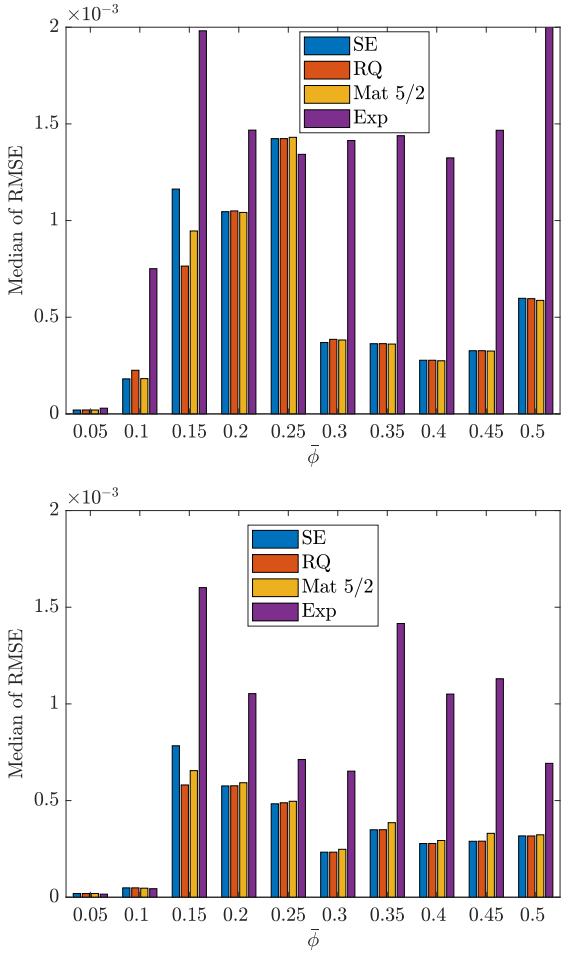

FIG. 1: The average performance of four Gaussian process regression models at predicting the surface area from the original scattering data. In the top panel, a training set size of twenty was used. In the bottom panel, a training set size of thirty was used. It should be noted that the y-axis in the top panel has been truncated to make it easier to compare to the y-axis in the bottom panel.

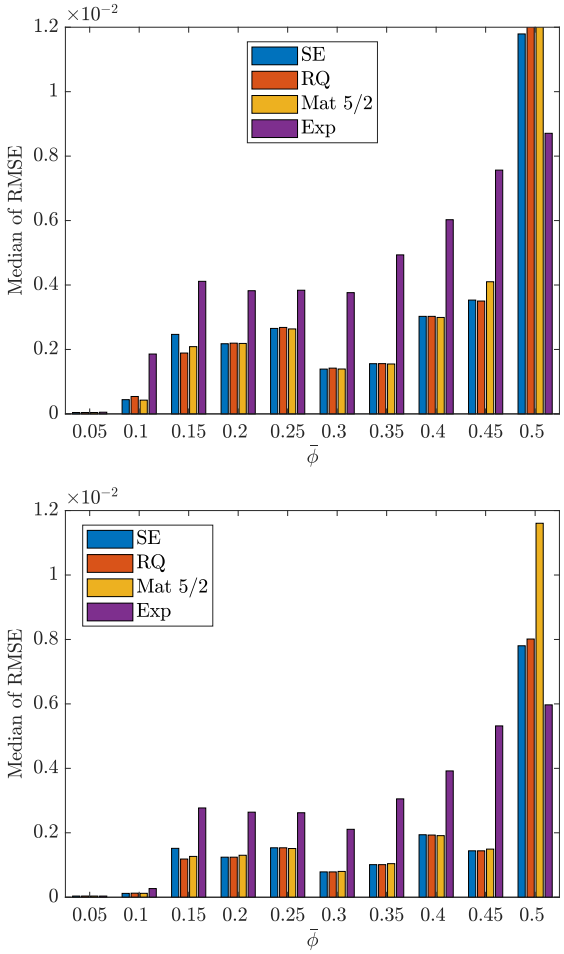

FIG. 2: The average performance of four Gaussian process regression models at predicting the curvature from the original scattering data. In the top panel, a training set size of twenty was used. In the bottom panel, a training set size of thirty was used. It should be noted that the y-axis in the top panel has been truncated to make it easier to compare to the y-axis in the bottom panel.

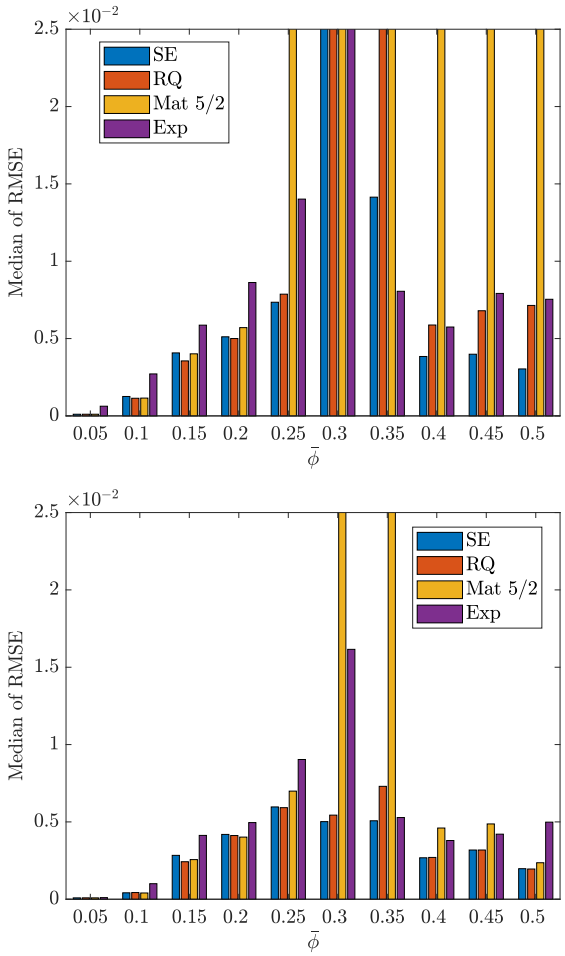

FIG. 3: The average performance of four Gaussian process regression models at predicting the connectivity from the original scattering data. In the top panel, a training set size of twenty was used. In the bottom panel, a training set size of thirty was used. It should be noted that the y-axis in the top panel has been truncated to make it easier to compare to the y-axis in the bottom panel. The y-axis in the bottom panel has also been truncated to make the bar chart easier to read.

B. Performance Summary of the Best Models

The performance of the best model for each value of $\bar{\phi}$ in the bottom panels of Fig. 3 in the paper and Figs. 1 - 3 here is shown in detail in Figs. 4-7, respectively. Each box plot summarises the values of the RMSE calculated over one hundred instances of training and testing.

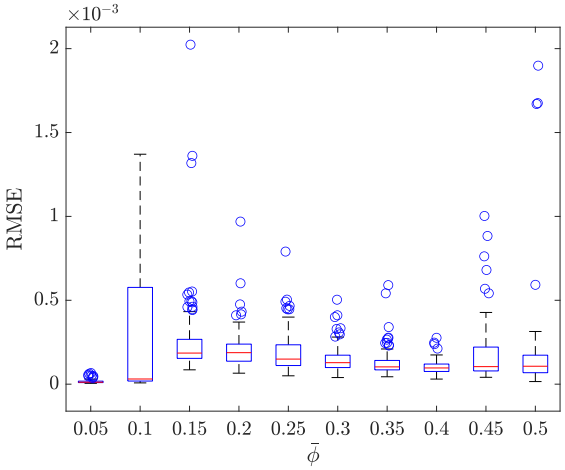

FIG. 4: The performance of the best Gaussian process regression models at predicting the volume from the original scattering data for each value of $\bar{\phi}$.

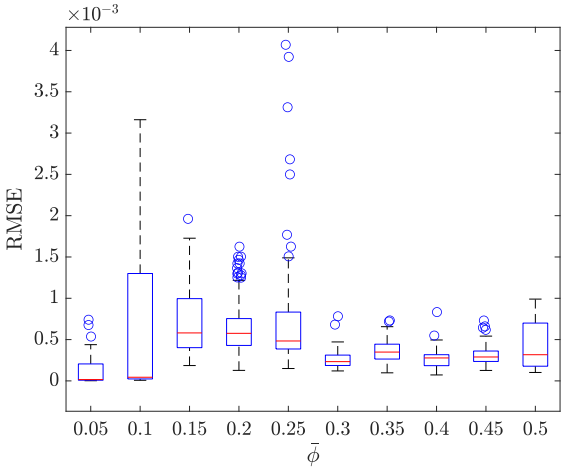

FIG. 5: The performance of the best Gaussian process regression models at predicting the surface area from the original scattering data for each value of $\bar{\phi}$.

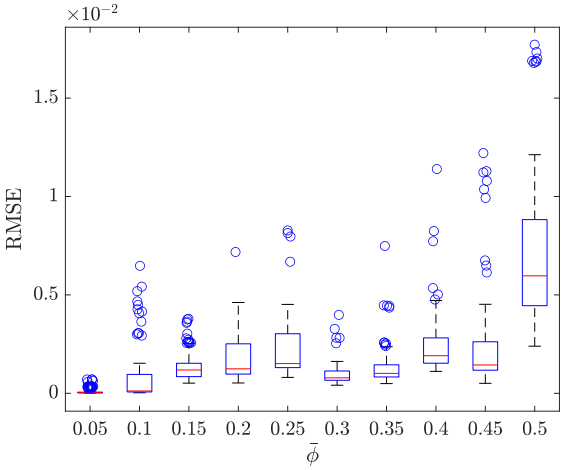

FIG. 6: The performance of the best Gaussian process regression models at predicting the curvature from the original scattering data for each value of $\bar{\phi}$.

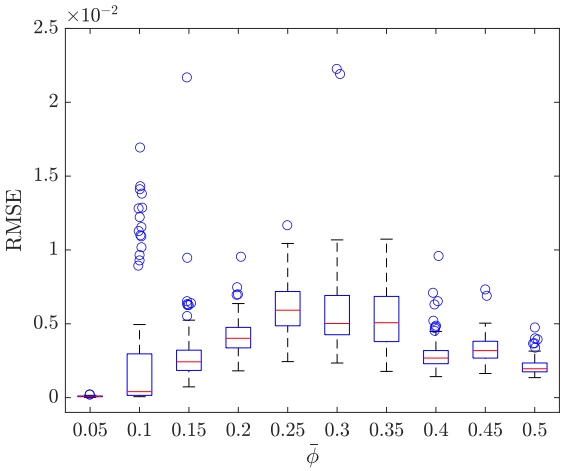

FIG. 7: The performance of the best Gaussian process regression models at predicting the connectivity from the original scattering data for each value of $\bar{\phi}$. It should be noted that the y-axis has been truncated to make the box plots easier to read. As a result of this, some of the outliers for $\bar{\phi} = 0.25$, 0.3 and 0.35 have been cut out.

IV. DEVELOPING THE NEURAL NETWORK

The neural network was set up and trained using Scikit-learn [9]. The training procedure was the same as that used for the Gaussian process regression models. On top of that, we made use of Scikit-learn's 'standard scaler' function. Before training the neural network, we determined the values of its hyperparameters by performing a grid search. The search was over the hidden layer sizes 128 and 256; the activation functions 'logistic', 'tanh' and 'relu'; the regularisation values (alpha)

0.0001, 0.001, 0.01 and 0.1; the solvers 'lbfgs', 'sgd' and 'adam'; and the maximum iteration values 250, 500 and 750.

[1] J. W. Cahn and J. E. Hilliard. Free Energy of a Nonuniform System. I. Interfacial Free Energy. *The Journal of Chemical Physics*, 28(2):258–267, 1958.

[2] J. W. Cahn. On spinodal decomposition. *Acta Metallurgica*, 9(9):795–801, 1961.

[3] J. W. Cahn. Phase Separation by Spinodal Decomposition in Isotropic Systems. *The Journal of Chemical Physics*, 42(1):93–99, 1965.

[4] Paul John Flory. *Principles of Polymer Chemsitry.* Cornell University Press, 1953.

[5] P. G. de Gennes. Dynamics of fluctuations and spinodal decomposition in polymer blends. *The Journal of Chemical Physics*, 72(9):4756–4763, 1980.

[6] S. C. Glotzer. Computer Simulations of Spinodal Decomposition in Polymer Blends. In *Annual Reviews of Computational Physics II*, volume 2 of *Annual Reviews of Computational Physics*, pages 1–46. World Scientific, 1995.

[7] Carl Edward Rasmussen and Christopher K. I. Williams. *Gaussian Processes for Machine Learning.* The MIT Press, 2006.

[8] D Duvenaud. *Automatic Model Construction with Gaussian Processes.* PhD thesis, University of Cambridge, 2014.

[9] Pedregosa *et al. Scikit-learn: Machine learning in Python.* Journal of Machine Learning Research*, 12:2825–2830, 2011.*